Supporting Information

Converting Silicon Nanoparticles into Nickel Iron Silicide Nanocrystals within Molten Salts for Water Oxidation Electrocatalysis

Yang Song, Sandra Casale, Antoine Miche, David Montero, Christel Laberty-Robert, David Portehault[*]

Table of contents

Electrode conductivity: comparison of related materials

Table S1 Comparison of the conductivity of reported OER electrocatalysts by their charge transfer resistances (R_{ct}) obtained from the electrochemical impedance spectroscopy (EIS).

Catalysts	R_{ct} (Ω)	Ref.
NiFeSi-12	17	This work
NiFeSi-50	5	This work
Ni-Fe disulfide	10	[1]
Ni-Fe hydroxide	17.5	[1]
$(Ni_{0.75}Fe_{0.25})_2P$	5	[2]
NiFe borate/rGO	38	[3]
NiFe borate	81	[3]
NiFe LDH/oGSH	100	[4]
NiFe LDH	1800	[4]
NiFe oxide	50	[5]
NiFe LDH/carbon network	353	[6]
NiFe LDH	875	[6]
NiFe LDH	70	[7]
$NiFe2O_4/Ni(OH)_2$	500	[8]

Chemicals

Reagents Lithium iodide (99%, Alfa Aesar), potassium iodide (99%, Sigma-Aldrich), silicon nanoparticles (99%, Nanomakers©, France), bulk Si powder (99 %, Sigma-Aldrich), nickel(II) chloride (99%, Alfa Aesar) and iron(II) chloride (99.5%, Alfa Aesar) were stored and manipulated as received in an Ar-filled glovebox (H_2O < 0.5 ppm, O_2 < 0.5 ppm). Methanol (VWR Normapur grade) was used for washing.

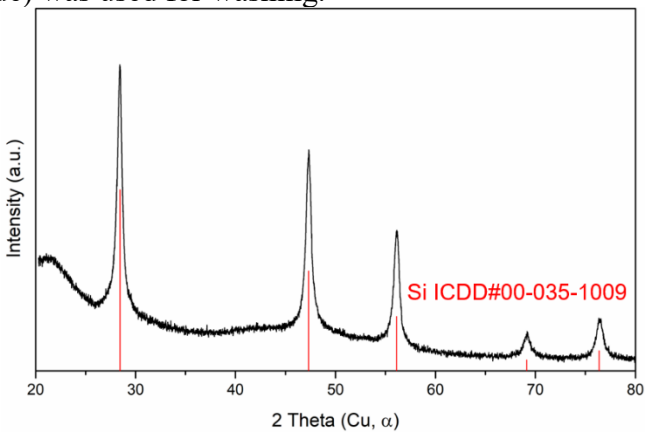

Figure S1. Powder XRD pattern of Si nanoparticles used as reagents. Red drop lines indicate a diamond-like structure Si reference.

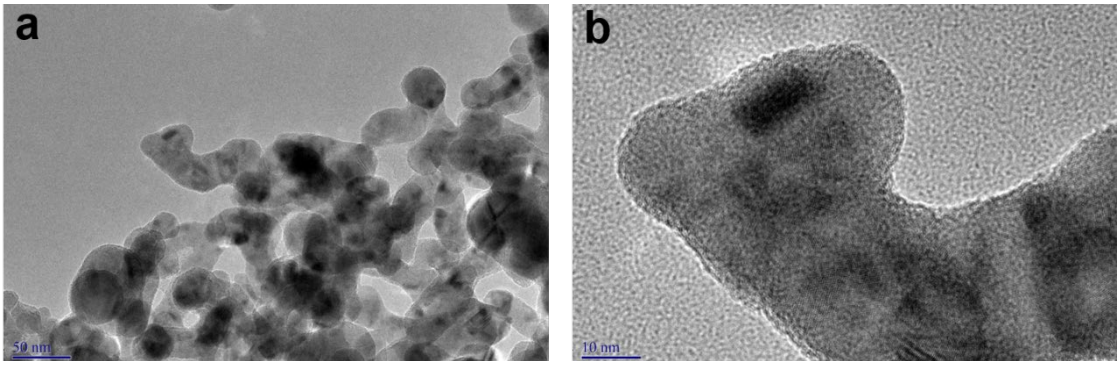

Figure S2. TEM images of Si nanoparticles used as reagents.

Instruments

Powder X-ray diffraction (XRD) diagrams were acquired on a Bruker D8 Advance diffractometer operating at the Cu Kα wavelength (λ = 1.5418 Å). *o*-Ni_2Si, *h*-Ni_2Si, FeSi, and NiOOH were identified according to the ICDD database and the reference cards 04-010-3516, 01-072-2547, 04-007-2551 and 00-06-0075 respectively.

X-ray photoelectron spectroscopy (XPS) analyses were performed using an Omicron Argus X-ray photoelectron spectrometer, equipped with a monochromated AlKα radiation source (1486.6 eV) and a 280 W electron beam power. Binding energies were calibrated against the C 1s (C-C) binding energy at 284.8 eV.

High-resolution transmission electron microscopy (HRTEM) was carried out on a JEOL JEM 2100 FEG microscope (Tokyo, Japan) operating at 200 kV with a spatial punctual resolution of 1.8 Å equipped with X-ray Energy Dispersive Spectroscopy (EDS) for chemical analysis. The samples were prepared by depositing a drop of ethanolic suspension on carbon coated Cu grids.

Analysis energy-dispersive X-ray spectroscopy (EDS) (Oxford Instruments – X-max) was performed on a scanning electron microscope (SEM) HITACHI S3400N at 20 kV. Cobalt was used for calibration of quantitative analyses. Powder samples were flatly smeared on a carbon adhesive tape on sample holder. Spectra were recorded on three to six different zones for each sample.

Scanning electron microscopy (SEM) was carried out on a Hitachi SU-70 FESEM. Postmortem electrodes were observed without any surface coating, accelerating voltage settings as indicated in images.

Synthesis method

Metal silicide nanoparticles Si nanoparticles, metal chloride $NiCl_2$, $FeCl_2$ or both, 2.9 g LiI (21.7 mmol) and 2.1 g KI (12.7 mmol) were ball-milled during 2 min at 20 Hz (Retsch MM400 ball mill airtight vial of 50 mL, filled with one steel ball of 62.3 g with a diameter of 23 mm) to get a well-mixed fine powder. Precise reactant amounts are listed in the **Table S1**. The mixture was loaded in a quartz tube (Ø28×H345 mm) which was then connected to a N_2-flowed Schlenk line. An intermediate liquid nitrogen trap between the quartz tube and the Schlenk line was set to condensate the volatile byproduct SiI_4. A vertical furnace from Eraly® was pre-heated to the reaction temperature. Afterward, the quartz tube was evacuated and placed into the furnace. The reaction medium was maintained at the targeted temperature for 6 hours under dynamic vacuum (10^{-3} mbar). Then, the hot quartz tube was taken out and cooled down to room temperature. The as-obtained mixture was washed in methanol by seven cycles of centrifugation/redispersion and was later dried in a Schlenk tube under vacuum. The resulting powder was transferred and stored in an Ar-filled glovebox. A typical synthesis yields about 100 mg of powders, which corresponds to a yield of about 90 %.

Table S2. Reactant masses, amounts and temperatures for syntheses of Ni, Fe and NiFe silicides

Samples	Reactant / mg (mmol)			Reaction temperature (°C)
	Si	$NiCl_2$	$FeCl_2$	
Ni_2Si	42.1 (1.5)	194.4 (1.5)	/	300
NiFeSi-50	52.5(1.9)	243.0 (1.9)	47.5 (0.4)	300
NiFeSi-12	42.1 (1.5)	146.0 (1.1)	47.5 (0.4)	300
NiFeSi-3	84.3(3.0)	194.4 (1.5)	190.1(1.5)	300
FeSi	63.2 (2.3)	/	190.1(1.5)	400

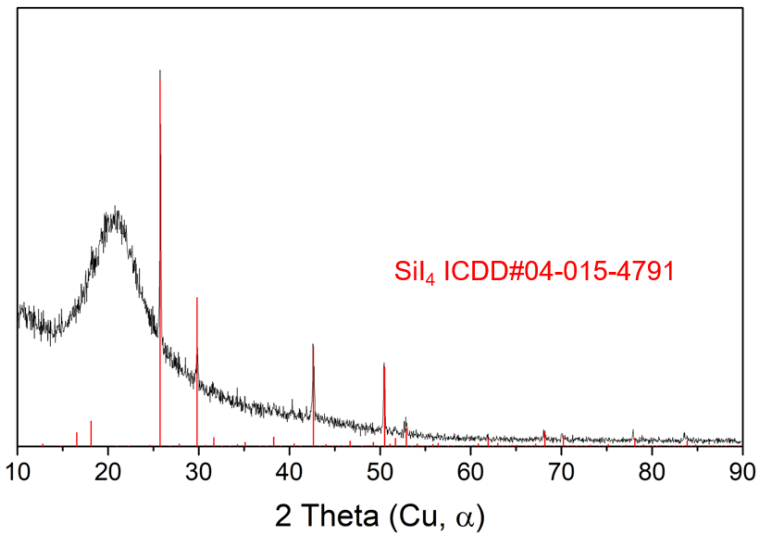

Figure S3. Powder XRD pattern of the byproduct of metal silicide synthesis, which can be indexed along the SiI_4 reference (indicated by red lines). The broad bumps between 15-25 ° come from the beam scattering of the protective PMMA plastic dome used for confining the Ar atmosphere around the sample.

Impact of synthesis parameters of Ni_2Si

Synthesis under Ar. 42.1 mg Si nanoparticles (1.5 mmol), 194.4 mg $NiCl_2$ (1.5 mmol) and 5 g LiI-KI (0.63:0.37 mol.) were ball-milled during 2 min. The same synthesis procedure was followed with the same setup as the synthesis described above, except that the reaction was under Ar flow instead of vacuum. The as-prepared solid was washed in methanol and in deionized water, respectively by six cycles and two cycles of centrifugation/redispersion, and was later dried under vacuum. The XRD diagram of final product is shown in **Figure S4**.

Synthesis from bulk Si powder. 42.1 mg bulk Si powder (1.5 mmol), 194.4 mg $NiCl_2$ (1.5 mmol) and 5 g LiI-KI (0.63:0.37 mol.) were ball-milled during 2 min. The synthesis protocol described above was kept. The as-obtained mixture was washed in methanol and in deionized water, respectively by six cycles and two cycles of centrifugation/redispersion, and was later dried under vacuum. The XRD diagram of final product is shown in **Figure S5**.

Synthesis without molten salts. 42.1 mg Si nanoparticles (1.5 mmol) and 194.4 mg $NiCl_2$ (1.5 mmol) were ball-milled during 2 min. Later, the same procedure was followed. After thermal treatment, the resulting powder was directly collected. The XRD diagram of final product is shown in **Figure S6**.

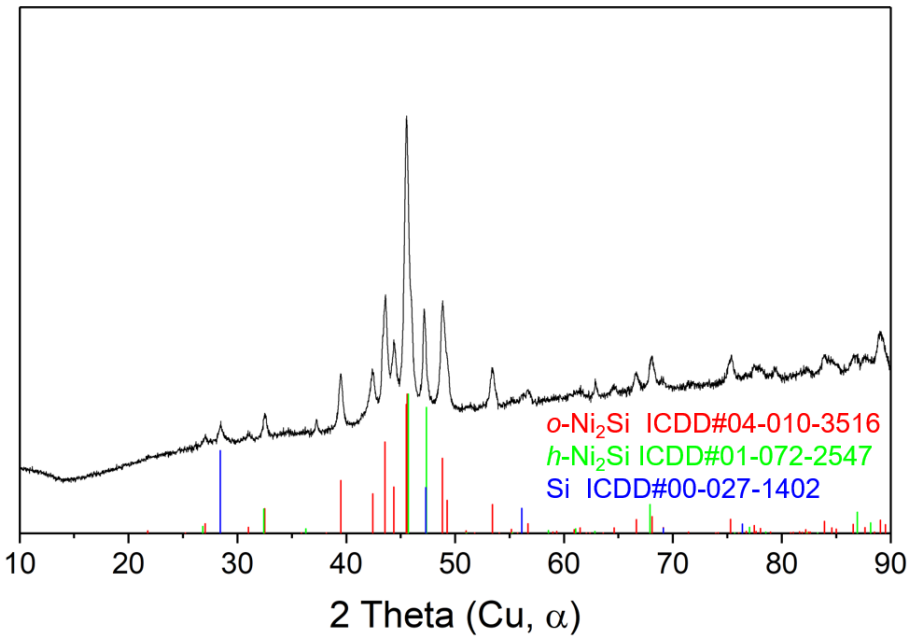

Figure S4. Powder XRD pattern of the final product from the reaction between Si nanoparticles and $NiCl_2$ under argon at 395°C for 6 hours in LiI-KI. Nickel silicides were the major phase, however unreacted Si can be observed.

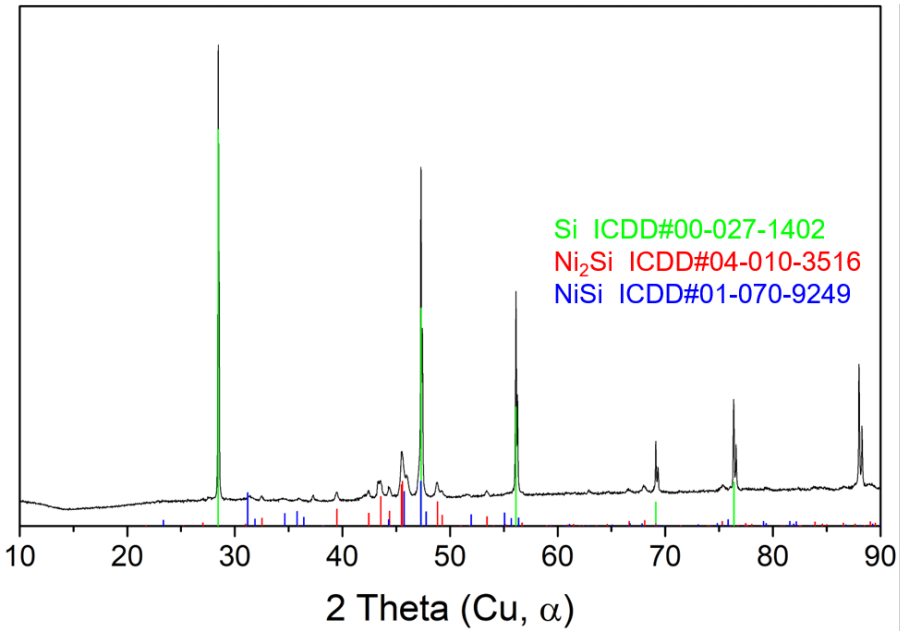

Figure S5. Powder XRD pattern of the final product from the reaction between bulk Si powder and $NiCl_2$ under vacuum at 395 °C for 6 hours in LiI-KI. Large amount of Si remains unreacted. Nickel silicides were formed in a minor fraction.

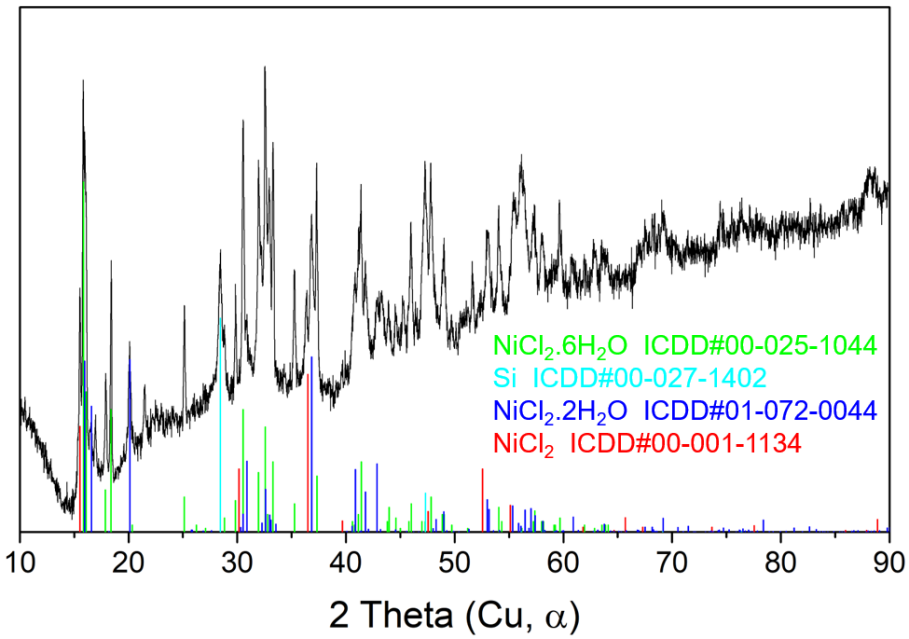

Figure S6. Powder XRD pattern of the final product from the solid-solid reaction between Si nanoparticles and $NiCl_2$ under vacuum at 395°C for 6 hours. Unreacted Si and $NiCl_2$ were found. $NiCl_2$ was hydrated because the XRD diagram was acquired in the air.

Characterization of metal silicide nanoparticles

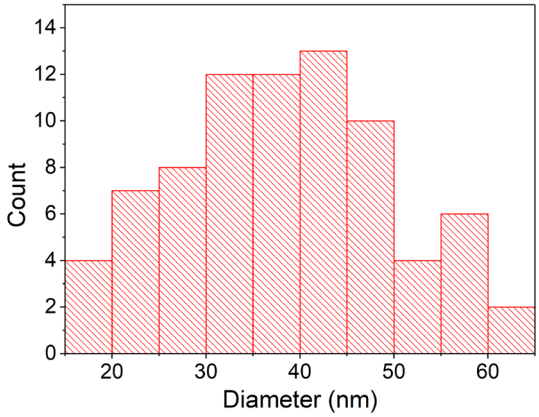

Figure S7. Size distribution of NiFeSi-12

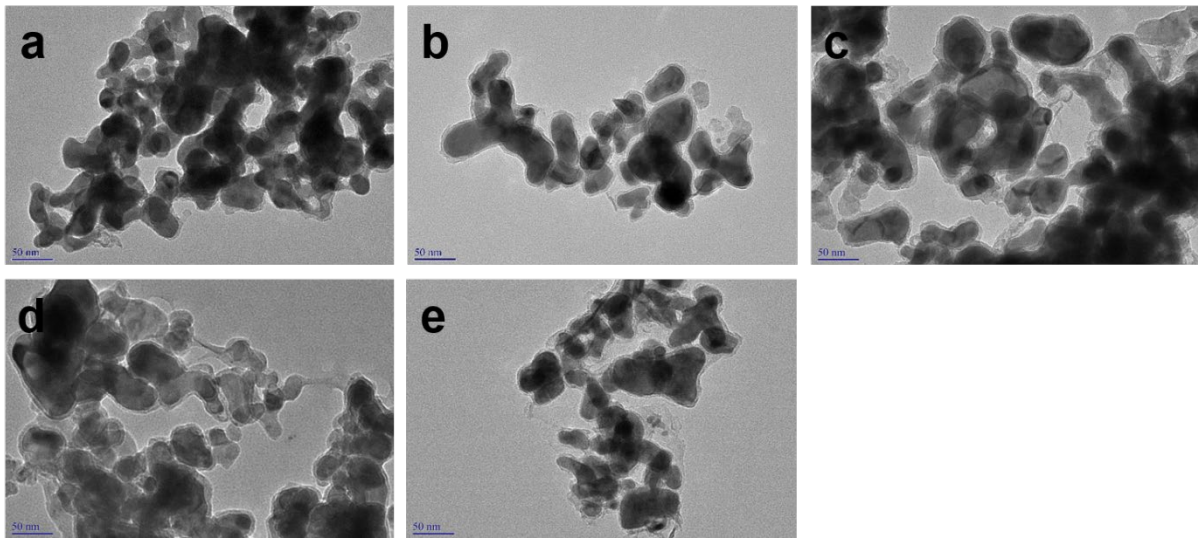

Figure S8. TEM images of (a) NiFeSi-50, (b) NiFeSi-12, (c) NiFeSi-3, (d) FeSi and (e) Ni_2Si.

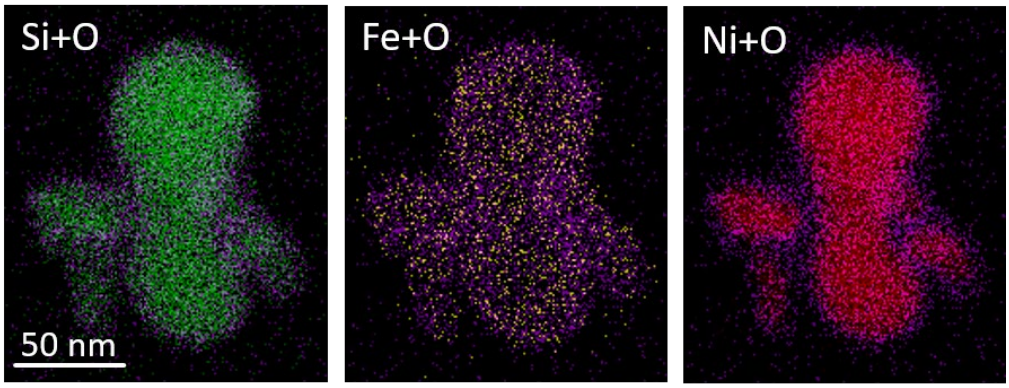

Figure S9. STEM-EDS mapping of the as-prepared NiFeSi-12 sample: superposition of oxygen and other elements. Si, Fe, Ni, O distributions are shown in green, yellow, red and purple, respectively.

Table S3. Elements atomic ratio of as-prepared Ni, Fe and NiFe silicide samples determined by EDX-SEM. The samples exhibit an excess of silicon compared to the composition expected from XRD phase identification. We then attribute this excess of silicon to amorphous silicon or oxidized silicon observed at the surface of the particles.

	Ni_2Si	NiFeSi-50	NiFeSi-12	NiFeSi-3	FeSi
Ni	1.68	1.96	1.85	0.84	/
Fe	/	0.04	0.15	0.31	0.58
Si	1	1.17	1.74	1	1

Electrochemical experiments

Electrode preparation. A Pt wire and Ag/AgCl in saturated KCl electrode were respectively used as counter electrode and reference electrode for a typical three-electrode configuration. There are two types of substrates used for the working electrode in this work. A glassy carbon (GC) rotating disk electrode (RDE) with a diameter of 5 mm was used for cyclic voltammetry (CV), linear sweep voltammetry (LSV) and electrochemical impedance spectroscopy (EIS) measurements, and a GC sheet was used for chronopotentiometry (CP) measurements. All catalyst inks were prepared with the same protocol. 3.4 mg of catalyst was sonicated in 480 μL absolute ethanol for 15 min, followed by adding 20 μL of Nafion solution (5% in alcohols and water, Sigma-Aldrich) for another 10 min of ultrasonication. A given volume of well-dispersed ink was dropped onto the GC sheet or the as-polished RDE substrate to obtain a catalyst loading of 170 $\mu g_{catalyst}/cm^2_{electrode}$, and then the substrate was dried for at least 30 min under air. IrO_2 nanoparticles were deposited according to the same protocol.

Electrolyte purification. *ca.* 1 g of as-prepared $Ni(OH)_2$ solid was put into 200 mL as-prepared 0.1M KOH. The suspension was sonicated for 3 min and then rested for at least 6 h. The purified 0.1M KOH supernatant was separated by centrifugation, stored under nitrogen and later used as electrolyte.

Electrochemical measurements. A home-made PMMA electrochemical cell was used for all measurements. The electrolyte was bubbled by O_2 for at least 20 min before measurement and during the measurement. The rotating rate of the RDE was set at 1600 rpm for all cyclic voltammetry (CV) measurements. CV and LSV measurements were performed at scan rate of 20 and 10 mV s^{-1}, respectively, from 0 to 1.0 V vs. Ag/AgCl in saturated KCl (equivalent to 1.0-2.0V vs. RHE). For the chronopotentiometry (CP), the current density was set at 10 mA cm^{-2} to monitor the potential evolution. Since a non-rotating GC sheet was used as working electrode substrate, a Teflon-covered stir bar stirred the electrolyte at 350 rpm during the measurements to decrease the limitation on activity due to ion depletion. The electrochemical impedance spectroscopy (EIS) was recorded in a frequency range of 50 000 to 1 Hz with a voltage amplitude of 10 mV.

Data treatment. For all potentials reported in this work, the ohmic drop iR was compensated, where the resistance is approximately equal to the total impedance measured at a frequency of 50 kHz. The potentials vs. RHE are obtained from conversion of measured potentials based on the equation: $E_{RHE} = E_{measured} + 0.197 + 0.0591 \times pH$, where pH = 13.

Cyclic voltammetry study

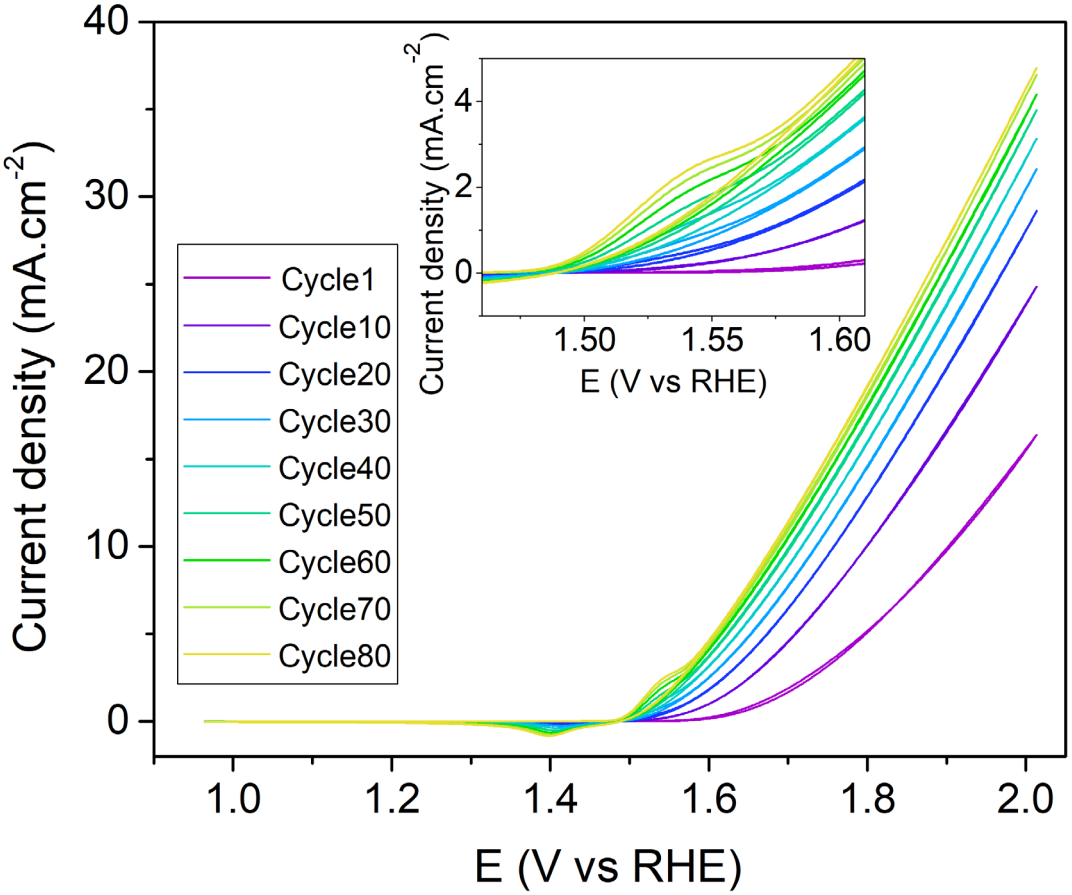

Figure S10. CVs for electrochemical activation of NiFeSi-12 by continuous potential cycling from 0.96 to 2.01 V vs. RHE at 20 mV s^{-1} in O_2-saturated 0.1 M KOH.

Electrochemical impedance spectroscopy study

In the Nyquist plots (**Figure S11**), the diameter of the semicircle in the high frequency region independent of the applied potential (**Figure S12**) represents the charge transfer resistance R_{ct}. The Fe-poor NiFeSi-50 exhibits the smallest R_{ct} (**Figures S11**). R_{ct} increases with the Fe content of NiFe silicides. The second semicircle in the low frequency region that decreases with the applied potential corresponds to R_{ads} (**Figure S12**). From **Figure S11,** the R_{ads} values are very close for the three NiFe silicides, which indicates similar surface states for these materials during electrocatalysis. The low values R_{ct}+R_{ads} (**Figures S10)** highlight the low overall resistances of NiFe silicide catalysts.

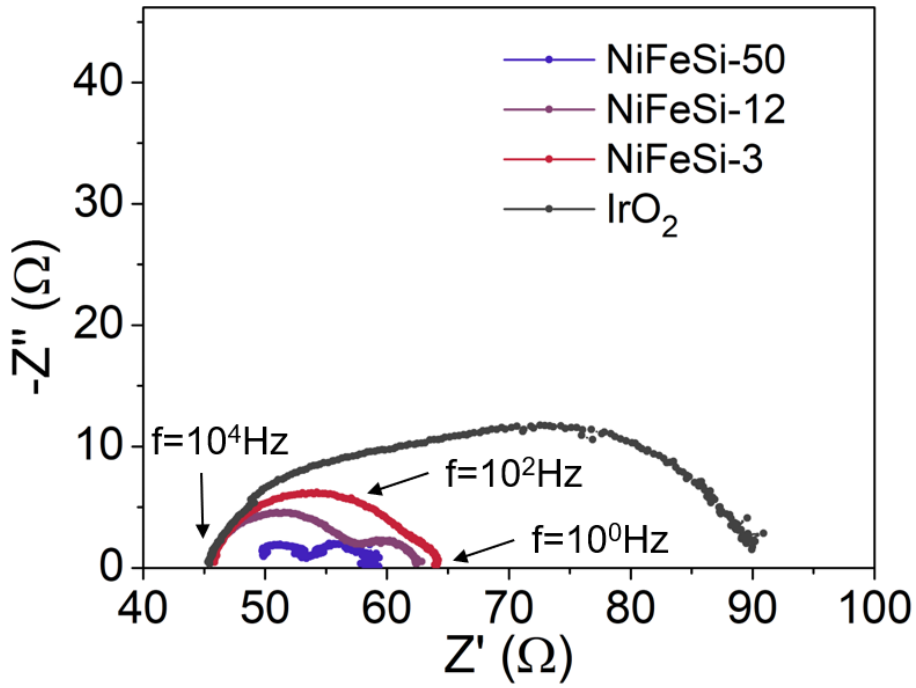

Figure S11. Nyquist plot recorded under 1.60 V vs. RHE of metal silicide nanocrystals and reference commercial IrO_2 nanoparticles in O_2-saturated 0.1 M KOH electrolyte.

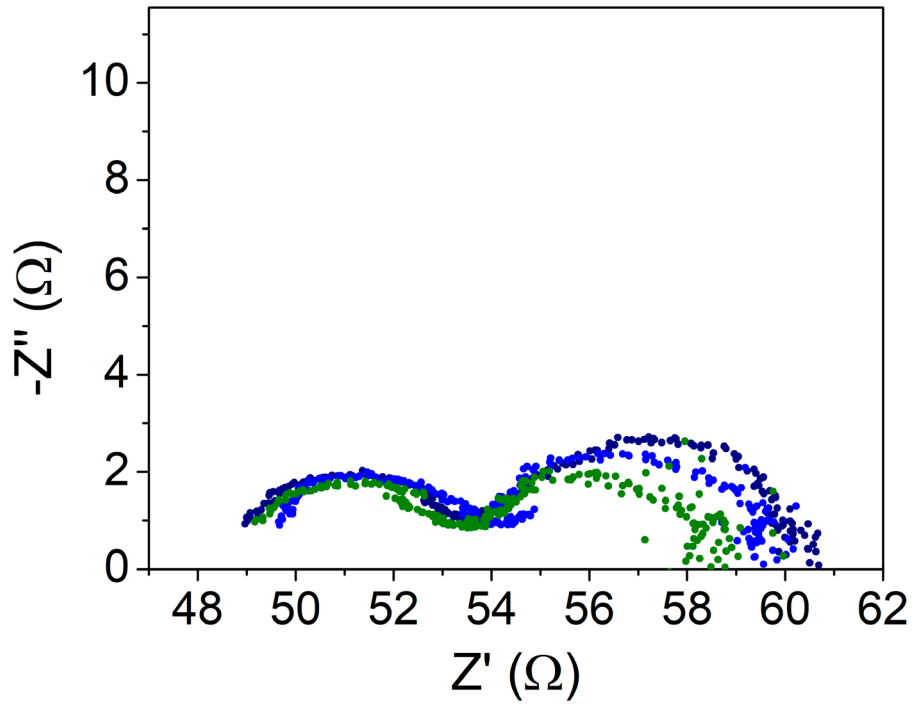

Figure S12. Nyquist plot of electrochemical impedance spectroscopy of NiFeSi-50 recorded at different potential from 50 000 to 1 Hz in green, blue, navy dots respectively, for 1.60 V, 1.59 V and 1.58 V vs. RHE**.**

Performance comparison of NiFe silicides with reported NiFe-based catalysts

Table S4. OER electrocatalytic activity and stability of previously reported NiFe-based catalysts in **0.1 M KOH** on **GC substrate**.

Catalyst	Loading amount (mg cm^{-2})	Overpotential (mV) @10mA cm^{-2}	Stability (h)	Tafel slope (mV dec^{-1})	Ref
NiFeSi-50	**0.17**	**337**	**85**	**63.8**	**This work**
NiFeSi-12	**0.17**	**345**	**85**	**85.4**	**This work**
NiFeSi-3	**0.17**	**393**	**85**	**75.3**	**This work**
nNiFe-LDH/NGF[a)]	0.25	337	3.3	45	[9]
Amorphous $Ni_{70}Fe_{30}(OH)_x$	0.14	292	2	30.4	[10]
$NiFe_2O_4$/α-$Ni(OH)_2$[b)]	~0.2	340	2.7	41	[8]
Ni_3FeN	~0.13	355	3.3	70	[11]
Fe^{3+}-doped β-$Ni(OH)_2$	0.25	260	10	32	[12]
NiFe-N/C[c)]	0.40	320	2000 cycles	44.2	[13]
NiFe-NC[d)]	0.20	380	2.8	115	[14]
graphene/NiFe (oxy)hydroxides	0.25	372	2.2	76	[15]
$Ni^{II}Fe^{III}$@NC	0.29	397	12	81	[16]
NiFe-LDH NS[e)]	0.14	290	8	33.4	[17]
Porous NiFe Oxide	0.14	328	12	42	[5]
$Ni_2Co^{III}Fe$-LDH/N-GO[f)]	0.18	317	8.3	74.1	[18]
Ni_3Fe/N-C	0.13	370	3.3	77	[19]
NiFe/C	0.50	330	21	57	[20]
m-NiFe/CN_x	0.51	360	5.6	59.1	[21]
NiFe LDH/oGSH[g)]	0.25	350	2.8	54	[4]
NiFe LDH	0.10	360	2	51	[22]
NiFe@NC_X	0.40	320	10	60.6	[23]

[a)] NGF: N-doped graphene framework
[b)] 0.1M NaOH
[c)] N/C: bimetal-decorated, pyridinic N-dominated large-size carbon tubes
[d)] NC: MM′ alloy and nitrogen-codoped porous carbon
[e)] NS: layered double hydroxide (LDH) nanosheets (NSs, ~ 1.3 nm)
[f)] N-GO: nitrogen-doped graphene oxide
[g)] oGSHs: oxidized graphene/ single-walled CNT hybrids

Table S5. Comparison of charge transfer resistance (R_{ct}) and mass transfer related to reaction intermediates adsorbed at the electrode surface (R_{ads}) for NiFeSi-12 electrodes in different stages of electrolysis.

Electrode	As-prepared	After 20 CVs	Post 85h-OER
R_{ct} (Ω)	6.2	5.3	5.2
R_{ads} (Ω)	15	6.9	0.1

Post mortem study of NiFe silicides

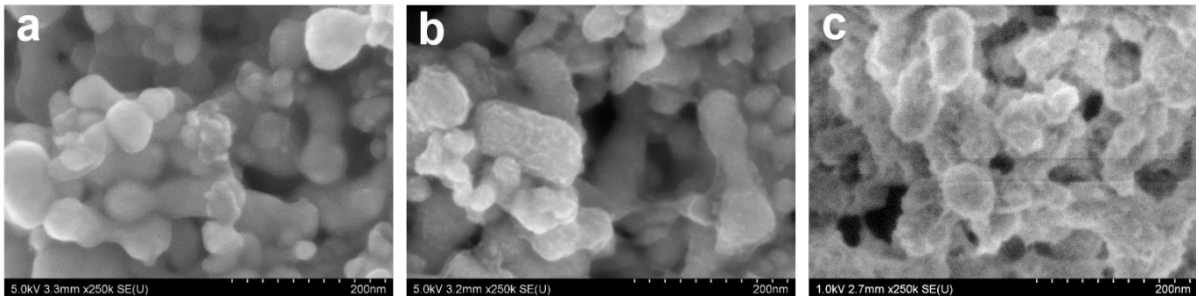

Figure S13. SEM images of a working electrode made of NiFeSi-12 nanoparticles deposited on a GC substrate (a) before electrochemical study, (b) post 10h OER, and (c) post 85h OER.

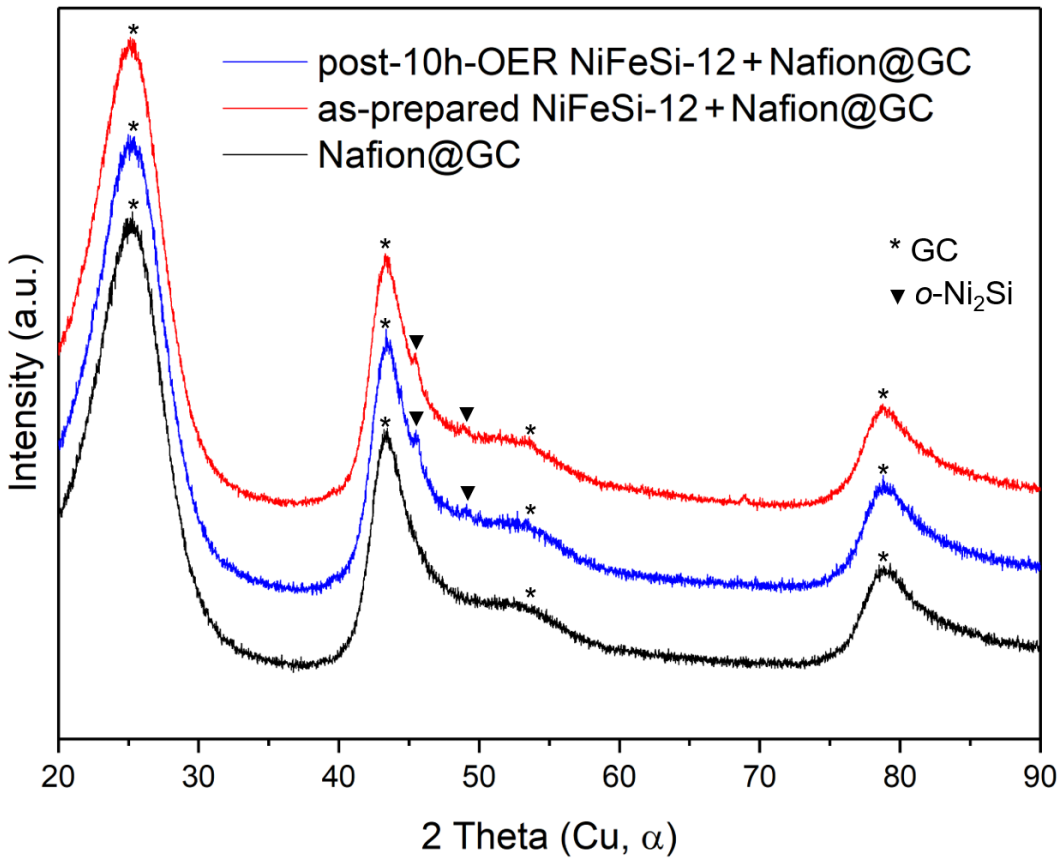

Figure S14. XRD patterns of a NiFeSi-12/glassy carbon electrode as-prepared and *post mortem* after 10 h of OER at 10 mA cm^{-2}. The pattern of a blank electrode without catalyst is shown as reference.

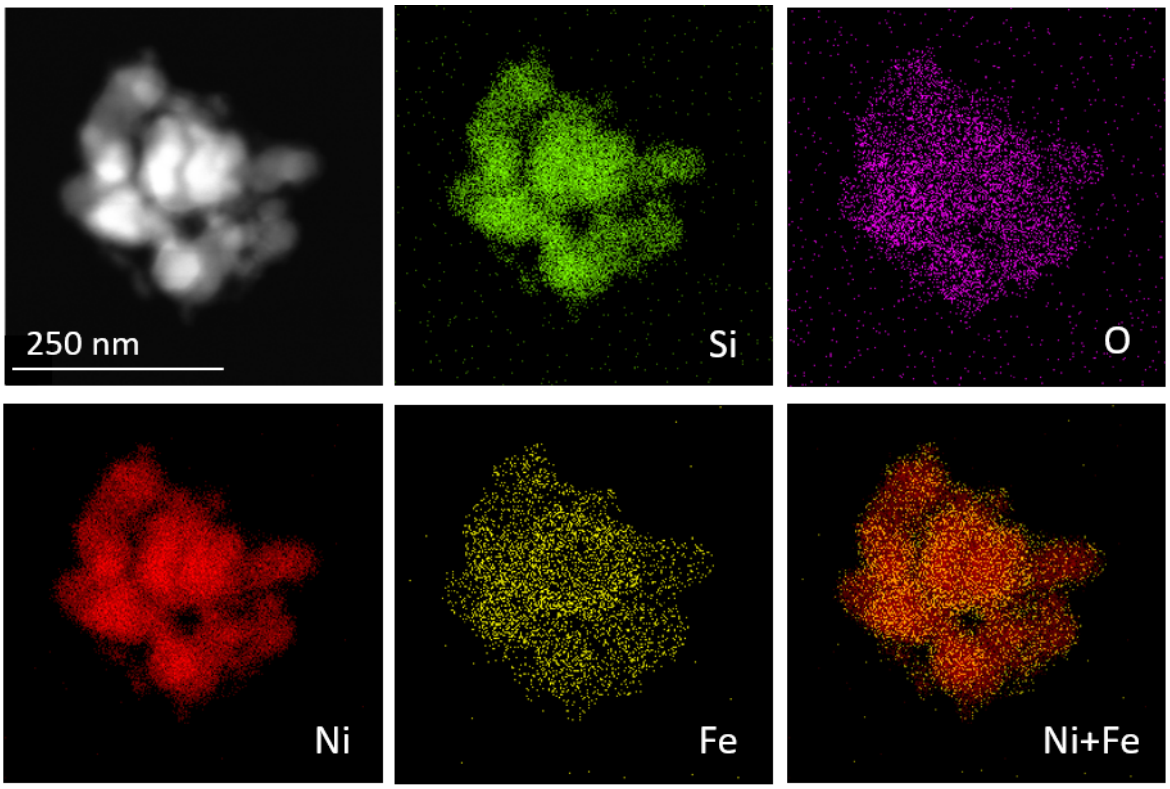

Figure S15. STEM-EDS mapping of NiFeSi-12 catalyst post 10h OER at 10 mA cm^{-2}.

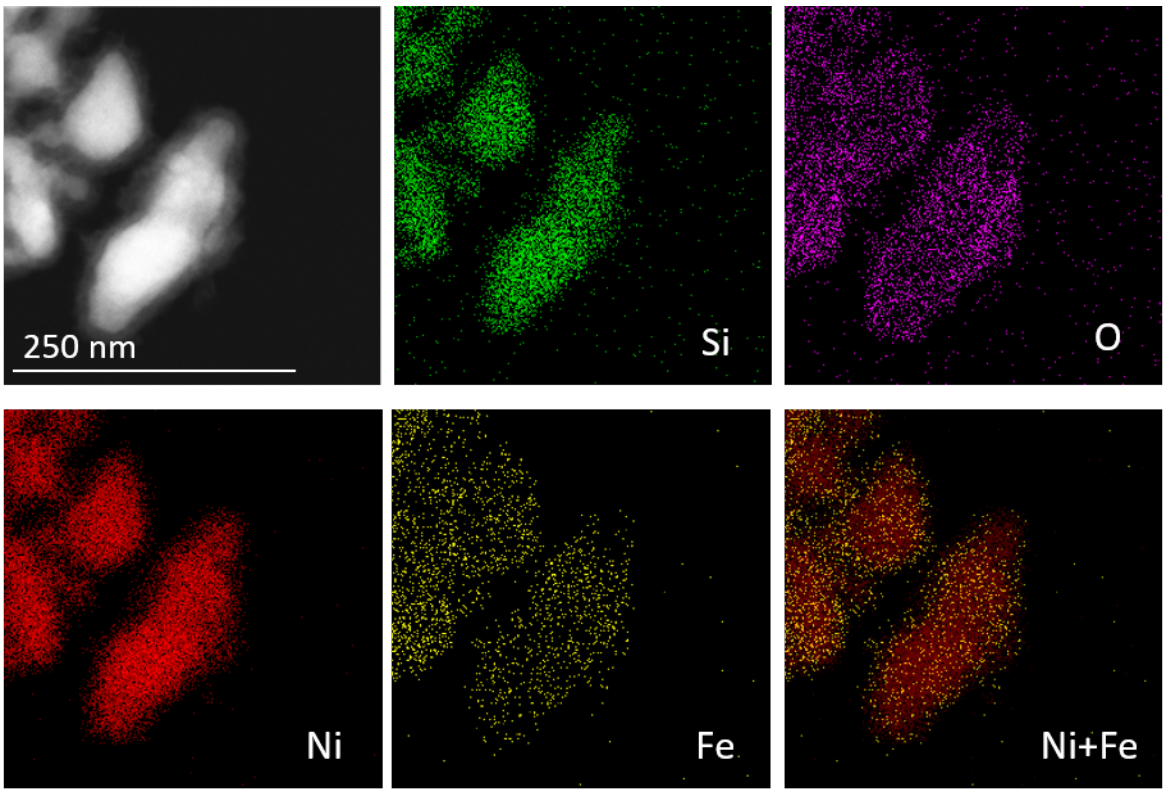

Figure S16. STEM-EDS mapping of NiFeSi-12 catalyst post 65h OER at 10 mA cm^{-2}.

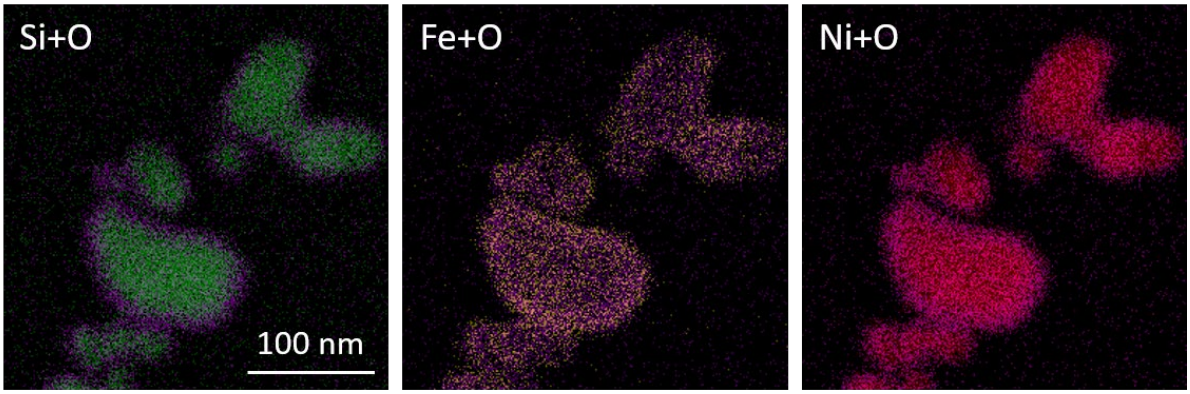

Figure S17. STEM-EDS mapping of NiFeSi-12 catalyst post 85h OER at 10 mA cm^{-2}: superposition of oxygen and other elements. Si, Fe, Ni, O distributions were shown in green, yellow, red, purple dots, respectively.

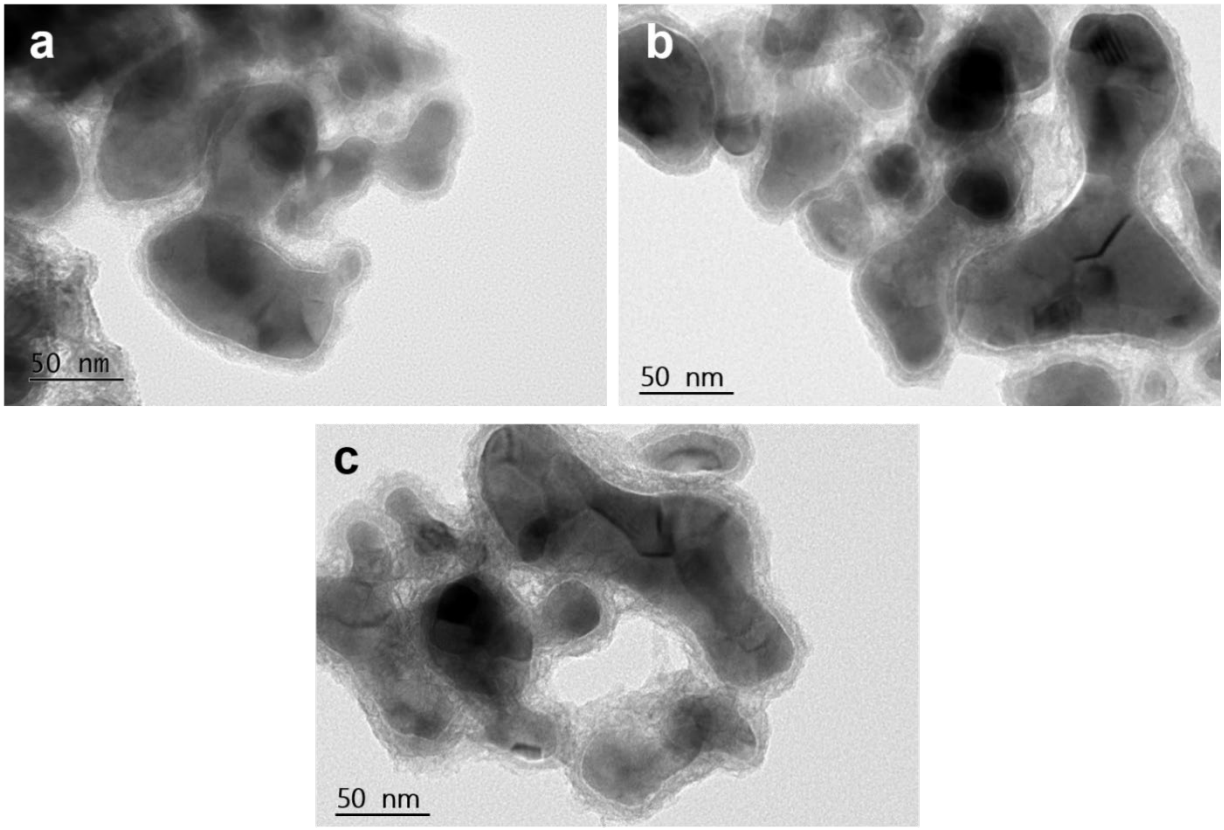

Figure S18. TEM images of NiFeSi-12 catalyst (a) post 10h OER, (b) post 65h OER, (c) post 85h OER at 10 mA cm^{-2}.

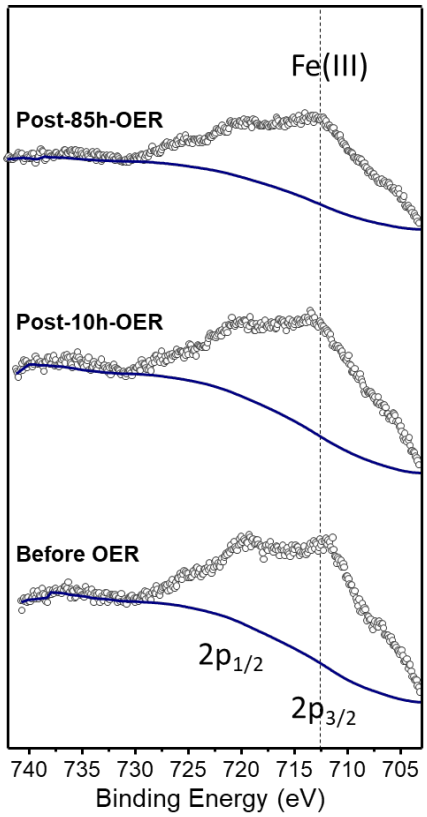

Figure S19. XPS analysis of the Fe 2p region for a NiFeSi-12 working electrode before OER, post 10h OER and post 85h OER.

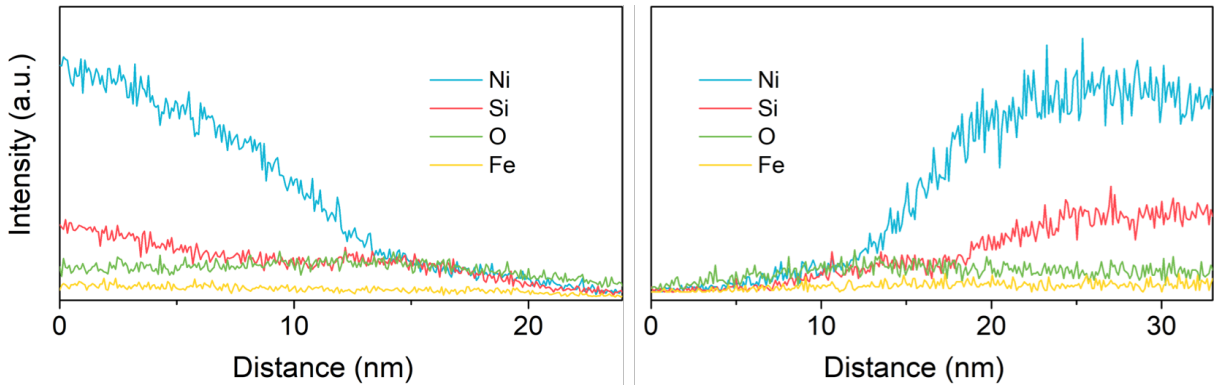

Figure S20. STEM-EDS line profile mapping of two NiFeSi-12 particles post 85h OER at 10 mA cm^{-2}.

Table S5. Elemental composition determined by SEM-EDS of a pristine NiFeSi-12 sample and of corresponding post mortem electrode materials after 65 and 85 h of OER operation.

	Pristine	Post 65h-OER	Post 85h-OER
Ni	1.85	1.85	1.85
Fe	0.15	0.12	0.11
Si	1.74	0.77	0.76

Supporting references

[1] C. Tang, H. Sen Wang, H. F. Wang, Q. Zhang, G. L. Tian, J. Q. Nie, F. Wei, *Adv. Mater.* **2015**, *27*, 4516.

[2] E. Lee, A. H. Park, H. U. Park, Y. U. Kwon, *Ultrason. Sonochem.* **2018**, *40*, 552.

[3] H. Chen, J. Yan, H. Wu, Y. Zhang, S. Liu, *J. Power Sources* **2016**, *324*, 499.

[4] G. Fu, Z. Cui, Y. Chen, L. Xu, Y. Tang, J. B. Goodenough, *Nano Energy* **2017**, *39*, 77.

[5] K. Zhu, H. Liu, M. Li, X. Li, J. Wang, X. Zhu, W. Yang, *J. Mater. Chem. A* **2017**, *5*, 7753.

[6] J. Wang, F. Ciucci, *Small* **2017**, *13*, 1.

[7] L. Yang, X. Zeng, D. Wang, D. Cao, *Energy Storage Mater.* **2018**, *12*, 277.

[8] C. Tang, H. F. Wang, H. Sen Wang, F. Wei, Q. Zhang, *J. Mater. Chem. A* **2016**, *4*, 3210.

[9] L. Du, L. Luo, Z. Feng, M. Engelhard, X. Xie, B. Han, J. Sun, J. Zhang, G. Yin, C. Wang, Y. Wang, Y. Shao, *Nano Energy* **2017**, *39*, 245.

[10] R. Gao, D. Yan, *Nano Res.* **2018**, *11*, 1883.

[11] J. Qi, W. Zhang, R. Xiang, K. Liu, H. Y. Wang, M. Chen, Y. Han, R. Cao, *Adv. Sci.* **2015**, *2*, 1.

[12] D. Zhou, Z. Cai, X. Lei, W. Tian, Y. Bi, Y. Jia, N. Han, T. Gao, Q. Zhang, Y. Kuang, J. Pan, X. Sun, X. Duan, *Adv. Energy Mater.* **2018**, *8*, 1701905.

[13] G. Fu, Z. Cui, Y. Chen, Y. Li, Y. Tang, J. B. Goodenough, *Adv. Energy Mater.* **2017**, *7*, 1.

[14] C. Andronescu, S. Barwe, E. Ventosa, J. Masa, E. Vasile, B. Konkena, S. Möller, W. Schuhmann, *Angew. Chemie - Int. Ed.* **2017**, *56*, 11258.

[15] S. Ci, S. Mao, Y. Hou, S. Cui, H. Kim, R. Ren, Z. Wen, J. Chen, *J. Mater. Chem. A* **2015**, *3*, 7986.

[16] X. Zhu, C. Tang, H. F. Wang, Q. Zhang, C. Yang, F. Wei, *J. Mater. Chem. A* **2015**, *3*, 24540.

[17] F. Dionigi, T. Reier, Z. Pawolek, M. Gliech, P. Strasser, *ChemSusChem* **2016**, *9*, 962.

[18] J. Zhu, M. Xiao, Y. Zhang, Z. Jin, Z. Peng, C. Liu, S. Chen, J. Ge, W. Xing, *ACS Catal.* **2016**, *6*, 6335.